SKIN CANCER DETECTION BY OBLIQUE-INCIDENCE DIFFUSE REFLECTANCE SPECTROSCOPY

A Thesis

by

ELIZABETH BROOKS SMITH

Submitted to the Office of Graduate Studies of
Texas A&M University
in partial fulfillment of the requirements for the degree of

MASTER OF SCIENCE

December 2006

Major Subject: Biomedical Engineering

SKIN CANCER DETECTION BY OBLIQUE-INCIDENCE DIFFUSE REFLECTANCE SPECTROSCOPY

A Thesis

by

ELIZABETH BROOKS SMITH

Submitted to the Office of Graduate Studies of
Texas A&M University
in partial fulfillment of the requirements for the degree of

MASTER OF SCIENCE

Approved by:

Chair of Committee,	Lihong Wang
Committee Members,	Gerard Cote
	Naisyin Wang
Head of Department,	Gerard Cote

December 2006

Major Subject: Biomedical Engineering

ABSTRACT

Skin Cancer Detection by Oblique-Incidence Diffuse Reflectance Spectroscopy.

(December 2006)

Elizabeth Brooks Smith, B.E., Vanderbilt University

Chair of Advisory Committee: Dr. Lihong Wang

Skin cancer is the most common form of cancer and it is on the rise. If skin cancer is diagnosed early enough, the survival rate is close to 90%. Oblique-incidence diffuse reflectance (OIR) spectroscopy offers a technology that may be used in the clinic to aid physicians in diagnosing both melanoma and non-melanoma skin cancers. The system includes a halogen light source, a fiber optic probe, an imaging spectrograph, a charge coupled device (CCD) camera, and a computer. Light is delivered to the skin surface via optical fibers in the probe. After interacting with the skin, the light is collected and sent to the spectrograph that generates optical spectra. Images and histopathological diagnoses were obtained from 250 lesions at the University of Texas M.D. Anderson Cancer Center (Melanoma and Skin Center). To classify OIR data, an image processing algorithm was developed and evaluated for both pigmented and non-pigmented lesions. The continuous wavelet transform and the genetic algorithm were employed to extract optimal classification features. Bayes decision rule was used to categorize spatio-spectral images based on the selected classification features. The overall classification accuracy for pigmented melanomas and severely dysplastic nevi is 100%. The overall

classification accuracy for non-pigmented skin cancers and severely dysplastic nevi is 93.33%. Oblique-incidence diffuse reflectance spectroscopy and the developed algorithms have high classification rates and may prove useful in the clinic as the process is fast, noninvasive and accurate.

ACKNOWLEDGEMENTS

I would like to express thanks to Dr. Lihong Wang for his teachings and support through my graduate studies. I would also like to show appreciation to Dr. Gerard Cote and Dr. Niasyin Wang for participating on my committee. Last but not least, I would like to express gratitude to Alejandro Garcia-Uribe for all of his assistance with data analysis.

TABLE OF CONTENTS

Page

LIST OF FIGURES

LIST OF TABLES

CHAPTER I

INTRODUCTION

1.1 Overview of Skin Cancer

Skin cancer is the most common form of cancer and it is on the rise. Non-melanoma skin cancers account for half of all cancers and include basal cell carcinomas and squamous cell carcinomas. Basal cell carcinomas begin in the basal cell layer of the epidermis. The tumor cells continue dividing but do not differentiate any further. Squamous cell carcinomas develop from dividing keratinocytes in a higher level of the epidermis. The American Cancer Society estimates that there will be 1 million new cases of non-melanoma skin cancers in the U.S. this year[1]. Melanoma is the most serious and fatal type of skin cancer. Melanoma skin cancers arise from melanocytes in the nueral crest. The American Cancer Society estimates that there will be 62,000 new cases of melanoma in the U.S. this year with 8,000 people dying of the disease[1]. Skin cancer is difficult to diagnose non-invasively as malignant skin lesions can closely resemble their benign counterparts.

There are many kinds of lesions that can be mistaken for skin cancer or vice versa. The most common types include common nevi (moles), dysplastic nevi, warts, seborrheic keratosis, and actinic keratosis. Common nevi are benign growths formed by clusters of

---

This thesis follows the style of Applied Optics.

melanocytes in the basal layer of the epidermis or the top layers of the dermis. Dysplastic nevi have atypical size, shape, and organization of cells. They are more likely to turn into melanoma than common nevi and are graded mild, moderate or severe. Mild and moderate dysplastic nevi do not have to be removed but should be watched closely. Severe dysplastic nevi are always removed completely as they have resemblance of melanoma. Warts are harmless skin growths caused by a virus. Often times they go away by themselves, though some may need treatment. Seborrheic keratoses are benign wart-like tumors that are very common in people over 40. Actinic keratosis is a precancerous skin tumor caused by sun exposure and known in some cases to turn into squamous cell carcinoma. Different lesion types can have similar characteristics furthering the problem in discriminating between them.

1.2 Current Methods of Diagnosis

If skin cancer is diagnosed early enough, the survival rate is close to 90%. Visual examination is used in the clinic to determine whether a skin lesion may be cancerous. ABCDE represents common guidelines that are helpful in identifying skin cancer. Asymmetry (A), irregular border (B), variety of colors (C), large diameter (D), and evolving lesions (E) are symptoms of melanoma. Accuracy is partially determined by practice, but even the most experienced physician will be unable to diagnose certain lesions as many features are shared by benign and malignant tumors. It remains crucial that non-melanoma, melanoma, and benign tumors be differentiated during early stages. Dermoscopy decreases skin refraction and improves resolution of epidermal structures

and the nevoscope uses polarized light for imaging of skin lesions. Both of these methods add to the physician's accuracy but still leave a considerable margin for error. Questionable lesions must be biopsied as histopathology is the gold standard for diagnosis. This leads to many unnecessary biopsies that can be painful, costly, and slow to yield results. A non-invasive accurate method of diagnosis is needed in the clinic.

CHAPTER II

BACKGROUND

2.1 Optical Imaging Basics

X-ray, MRI, and ultrasound are imaging modalities commonly used in medical practice. Optical imaging is new to the field and has many interesting advantages. (1) Optical photons are non-ionizing offering a technology that is safe for patients. (2) Optical spectra are related to molecular conformation of biological tissue. (3) Optical absorption is related to angiogenesis, hyper-metabolism, and cell death. (4) Optical scattering can be used to measure the size of scattering particles. (5) The Doppler Effect can be used to image blood flow. This research analyzes optical spectra of diffusely reflected light to discriminate between benign and cancerous tumors.

When light interacts with biological tissue, photons can be reflected, absorbed, scattered, or transmitted. Light that is immediately reflected when hitting the surface of the medium is termed specular reflectance. Photons that go through a series of absorption and scattering events before being reemitted at the top and bottom of the medium are considered diffuse reflectance and transmittance, respectively. Absorption is when energy is deposited into the medium as an electron is moved from the ground state of a molecule to the excited state. A scattering event occurs when a photon is deflected into a new direction. When photons first enter the medium, they are considered to be in the

ballistic regime as they are mostly forward directed. Once they begin to scatter in different directions isotropically, they are in the diffusion regime.

Biological tissue is considered scattering media as there is little absorption. Biological scatterers are primarily cell nuclei and mitochondria, with diameters ranging from 1 μm to 8 μm. The wavelengths used for this research are smaller than these scatterers, so the light interaction can be predicted by Mie scattering theory, which is an exact analytical solution of Maxwell's electromagnetic field equations. When the scattering particles are much smaller than the wavelength, the light interaction can be predicted by Raleigh scattering theory, which is a limiting case of Mie theory. Scattering coefficient is defined as the probability of photon scattering per unit infinitesimal pathlength.

In the visible range, the most significant absorbers in biological tissue include oxygenated hemoglobin, deoxygenated hemoglobin, and melanin. The concentration of each absorber can be calculated by measuring the absorption at different wavelengths. Absorption coefficient is defined as the probability of photon absorption per unit infinitesimal pathlength. When light propagates along x through an absorbing medium with absorption coefficient μ_a, the intensity varies according to Equation 2.1

$$I = I_0 \exp(-\mu_a x) \tag{2.1}$$

where I_0 is the initial intensity. This is commonly known as Beer's Law.

The Monte Carlo technique is very useful for simulating light propagation in tissue. Based on random movement, a large number of photon packets are traced yielding an accurate model of photon transport. A grid system can be used to store the absorption, diffuse reflectance, and transmittance quantities. Each photon packet is launched from the same location with a weight of one. Once hitting an interaction site, a fraction of the light is absorbed. The dropped weight is recorded and the weight is updated. The remaining portion continues to propagate through scattering events determined by statistically sampling the probability distributions for step size and deflection angle. If a packet hits a boundary, it can be internally reflected or transmitted based on probability. The weight of transmitted light is recorded. If a photon packet is transmitted at the surface of the tissue, the weight is recorded in the diffuse reflectance grid. When a photon packet exits the medium or the weight becomes too small, it is considered dead and a new photon packet is launched. This is continued to obtain a realistic representation of light propagation.

2.2 OIR History

Oblique-incidence reflectometry (OIR) can separate absorption and scattering properties based on relative measurements whereas normal-incidence reflectometry requires absolute measurements that can be difficult to obtain. OIR breaks the symmetry in the diffuse reflectance pattern resulting in a more robust clinical system. The setup incorporating oblique incidence light continues to evolve. Early research of oblique-incidence reflectometry tested the application of diffusion theory by comparing Monte

Carlo simulations and experimental results from a video reflectometer[2]. The next trial implemented a fiber optic probe[3], which was soon followed by the addition of the spectrograph[4]. Lastly, the probe was modified in size to be more appropriate for skin cancer, data acquisition was made to be real time, and clinical tests were performed.

The Optical Imaging Lab at Texas A&M University developed the first OIR imaging system. Garcia-Uribe et al.[5] classified non-pigmented lesions as benign or cancerous with 100% accuracy and pigmented lesions as benign or dysplastic with 95% accuracy. These results are very encouraging in that OIR technology in the clinic could greatly reduce the number of unnecessary biopsies. They were unable to include melanoma due to the size of the study, 102 lesions. The proposed research will use the same technology and methods but will be larger to ensure that melanoma is included in the classification algorithm.

2.3 Work by Others

Spectroscopic methods

Other researchers are also exploring the capabilities of spectroscopy to aid the physician in skin cancer detection. Wallace et al.[6,7] used multivariate discriminate analysis and neural networks to classify reflectance spectra of common nevi and melanoma. They reported an accuracy rate of 86.7% for the neural network technique though the study did not include dysplastic nevi. McIntosh et al.[8] utilized near-infrared reflectance spectroscopy with multivariate analysis to group spectra from non-melanoma skin

cancers, pre-cancers, and benign lesions. They described classification accuracies of 72.4-97.7%,. Tomatis et al.[9] discriminated between melanoma and non-melanoma lesions with 85% accuracy using multispectral imaging. Sigurdson et al.[10] employed Raman spectroscopy and neural networks to categorize skin lesions, including melanoma with a classification performance of 80.5%. Panjehpour et al.[11] used fluorescence spectroscopy to classify non-melanoma skin cancers and reported that it only worked well in patients with fair skin. The reports mentioned differentiate between the specified skin lesion classes, but none of them include melanoma skin cancers, non-melanoma skin cancers, atypical lesions, and benign lesions in one study. In the clinic, in would be most useful to be able to use one imaging modality on all questionable lesions.

Other methods

Non-spectroscopic methods also have some interesting results. Confocal scanning microscopy can image nuclear, cellular, and architectural detail in the epidermis and superficial dermis of melanocytic lesions[12,13]. This is only useful for pigmented lesions as the melanin causes the cytoplasm to appear bright. Analysis of cytologic structure makes it possible to discriminate between uniform cells of melanocytic nevi and atypical cells characteristic of melanoma. Aberg et al.[14] employed multi-frequency electrical impedance to categorize lesion types by the impedance relation between lesion and reference skin. Voltage was applied thorough two outer electrodes on a handheld probe and sensed with a center electrode. They were able to identify actinic keratosis and non-

melanoma skin cancers from benign nevi with 98.3% accuracy and melanoma from benign nevi with 89.0% accuracy.

Takahashi et al.[15] applied magnetic resonance imaging (MRI) to establish that the signal intensity accessed by the tumor-to-fat contrast ratio on T2-weighed images clearly differentiated between melanoma and benign pigmented lesions. Maurer et al.[16] added that melanoma had a higher SNR in both unenhanced T2-weighted and contrast enhanced fat suppression images, as well as a higher CNR in fat suppression sequences. More recently, Pennasilico et al.[17] utilized MRI with the contrast agent, gadopentetate dimeglumine, to evaluate parameters that may be used to differentiate between melanoma and benign lesions. The enhancement rate in the first minute was found to be significantly greater for melanomas and the signal-time intensity curves for melanoma were different than those for benign lesions. The mention MRI parameters provide limited differentiation ability at this time.

As discussed previously asymmetry is a distinguishing attribute of melanoma. Using symmetric distance variations and a backpropagation neural network, Ng et al.[18] have sorted symmetrical and asymmetrical lesions with 80% accuracy. This technique may prove useful though they have not yet tried to classify lesions. Piantanelli et al.[19] studied fractal analysis of boundary irregularity to find an increasing linear regression from common nevi to dysplastic nevi to melanomas. Common nevi and melanoma may be distinguished using this method, but there is too much overlap to separate dysplastic

nevi. The fractal dimension may be valuable when used in combination with other diagnostic parameters. Though research is moving forward, there is still a need for a device that can discriminate all types of lesions with high accuracy.

CHAPTER III

EXPERIMENTAL SETUP

The OIR system includes a light source, optical multiplexer, fiber optic probe, imaging spectrograph, charge coupled device (CCD) camera, and computer (Figure 1). The 150 W halogen light source (Fiberoptics Incorporated, SOL-R 150DC) provides stable white light output with negligible ultraviolet light. The optical multiplexer (Ocean Optics, MPM-2000) illuminates five source fibers one at a time. The aluminum probe was custom made by Ocean Optics consisting of five source fibers and 24 collection fibers. 200 μm plastic-clad silica source fibers were positioned linearly as shown in Figure 2. When the probe is placed perpendicular to the area of interest, the center source fiber is normal to the surface of incidence. The outer source fibers are situated at 45 degrees and

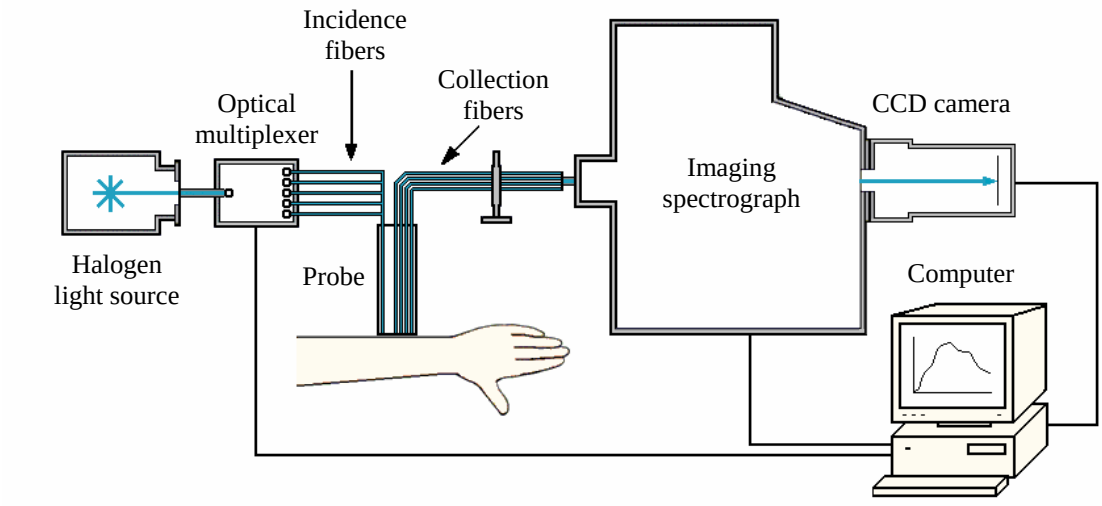

Figure 1. Schematic of OIR system

the remaining source fibers are at 25 degrees. Once the light is delivered to the area of interest, it interacts with the medium and the diffuse reflectance is collected by detection fibers. The custom made fiber bundle (Fiberguide Industries) consists of 100 μm silica-

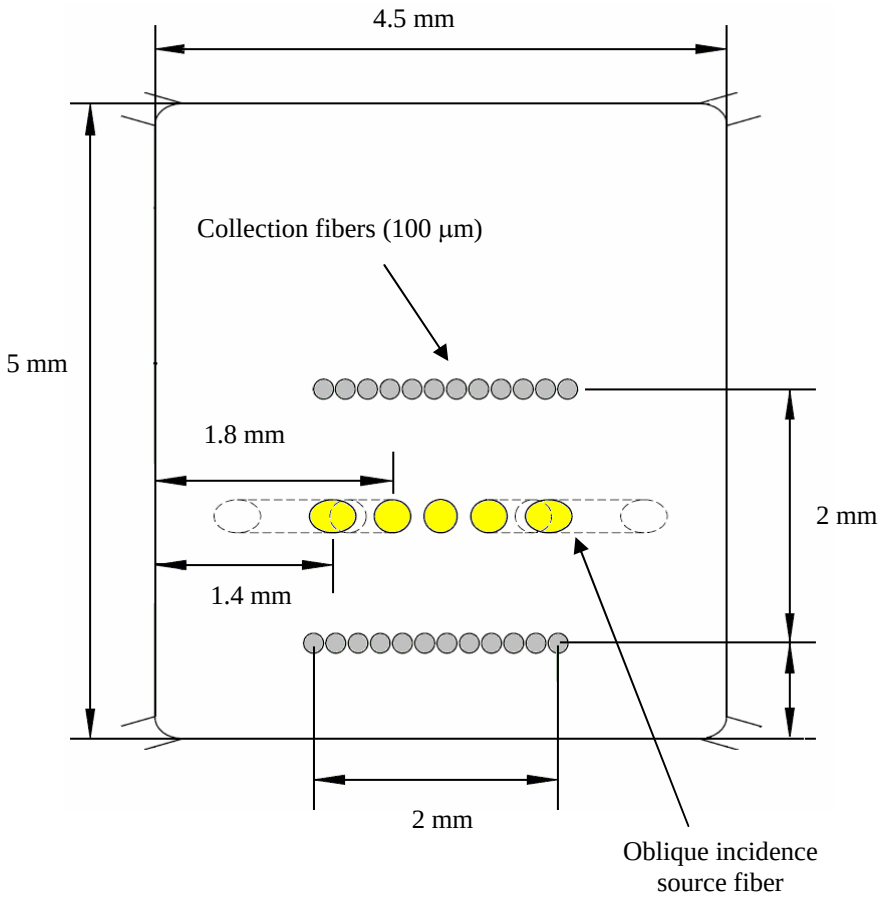

Figure 2. Diagram of probe tip

silica collection fibers that form two linear arrays on the probe tip. The fiber bundle is connected to the imaging spectrograph (Newport, Oriel MS 257) that disperses light into its component wavelengths and captures the optical spectra with a CCD camera. The

CCD chip has a 512 x 512 pixel chip that measures 12.3 x 12.3 mm^2. To prevent overlapping, 21 fibers were fit to the CCD chip with 3.6 nm resolution. The specifications of the spectrograph and CCD chip allow for a 290 nm wavelength range, which was selected to be 455 – 765 nm. Light in the visible range is best for this application because ultraviolet light is unsafe for patients and infrared light is not as sensitive for this purpose. Spatio-spectral images are automatically saved on the computer future data analysis. The system is built on portable cart that can be easily moved from room to room (Figure 3).

Figure 3. Picture of OIR system

CHAPTER IV

PRELIMINARY EXPERIMENT

4.1 Calibration and Validation

The system was calibrated and validated using liquid phantoms prepared with varying amounts of Trypan blue as the absorbers and polystyrene microspheres as the scatterers. A spectrophotometer used collimated transmission to measure the absorption coefficient for each phantom. The reduced scattering coefficient was calculated using Mie theory[20], which is based on known parameters of the microspheres. Three phantoms with different optical properties were used to calibrate the system. The diffuse reflectance was collected from each phantom by gently immersing the probe tip with the collection fibers normal to the surface. Calibration factors for each fiber and phantom were averaged and recorded for future data collection. In the same manner, the diffuse reflectance was collected from three additional phantoms to validate the system by extracting optical properties. Diffusion theory or scalable Monte Carlo can be used to calculate the absorption and scattering coefficients. The optical properties chosen for the phantoms allowed the diffusion theory method. The experimental and expected results are shown in Figure 4 at varying wavelengths. The absorption and scattering properties have good agreement.

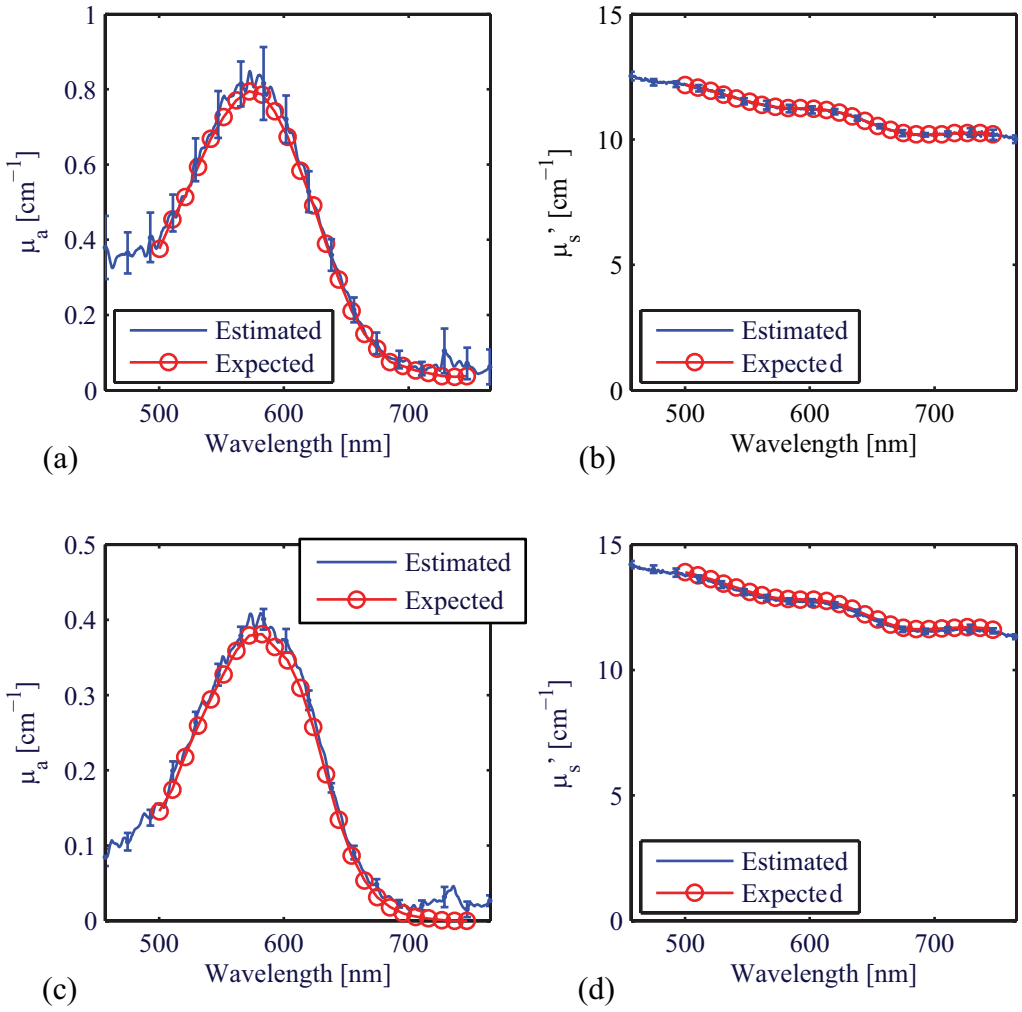

Figure 4. Expected and estimated optical properties (a) Absorption coefficient for phantom 1, (b) scattering coefficient for phantom 1, (c) absorption coefficient for phantom 2, (d) scattering coefficient for phantom 2

4.2 Diffusion Theory

Diffusion theory is based on the diffusion approximation[2] of the transport equation where the diffuse photon intensity is assumed to be uniform in all directions. The

fluence rate distribution from a point source can then be solved under the same approximation. Calculation of the absorption and scattering coefficients is derived from the modified diffusion theory-based model, though it does not accurately model "near diffuse reflectance", reflectance in the range of 1 transport mean free paths (mfp') of the source[21]. This problem can be avoided by only using "far diffuse reflectance," beyond 1 mfp' of the source. The optical properties for the phantoms were chosen so that the mfp' would be less than distance between the source and collection fibers. For normally incident light, the diffuse reflectance is modeled by two isotropic point sources; one positive source located below the tissue surface and one negative located above the tissue surface. For oblique incidence (Figure 5), the positive point source is the same distance from the incident light, but the tissue depth is modified by Snell's Law.

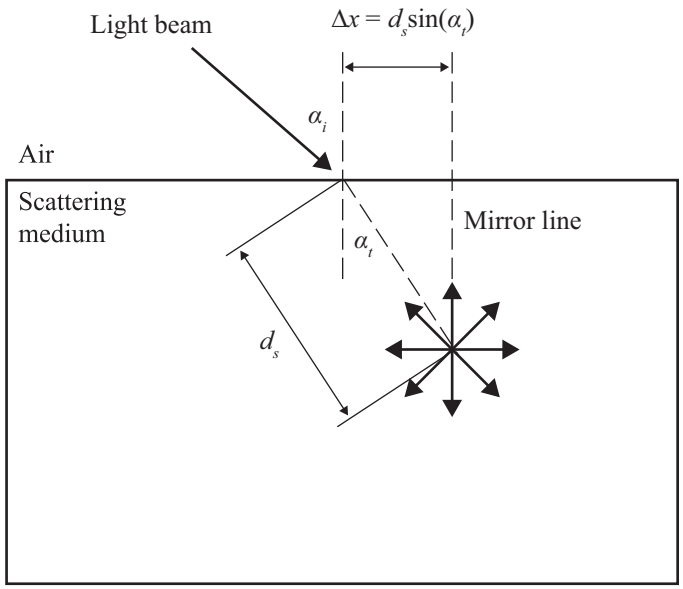

Figure 5. Schematic of obliquely incident light

According to Wang and Jacques[22], the distance from the point of incidence to the positive point source (d_s) is defined by

$$d_s = 3D = \frac{1}{0.35\mu_a + \mu_s'} \tag{4.1}$$

where μ_a is the absorption coefficient, μ_s' is the reduced scattering coefficient, and D is the diffusion coefficient. When using oblique incidence, there is a shift of the point sources in the x direction. Using elementary geometry, the shift (Δx) is defined by

$$\Delta x = d_s \sin(\alpha_t) = \frac{\sin(\alpha_t)}{0.35\mu_a + \mu_s'} \tag{4.2}$$

where α_t is the angle of refraction. Diffuse reflectance can be measured at multiple wavelengths. The position of the diffuse reflectance from the incident light can be obtained from the reflectance profile at a particular wavelength. Figure 6 shows the normalized reflectance profile at the wavelength of 576 nm for absorption and scattering coefficients of 0.39 cm^{-1} and 12.77 cm^{-1}, respectively. The diffuse reflectance can be calculated by the modified two-source diffusion theory model[4],

$$R(x) = (1 - R_s)a' \frac{1}{4\pi}\left[\frac{\Delta z(1+\mu_{eff}\rho_1)\exp(-\mu_{eff}\rho_1)}{\rho_1^3} + \frac{(\Delta z + 2z_b)(1+\mu_{eff}\rho_2)\exp(-\mu_{eff}\rho_2)}{\rho_2^3}\right] \tag{4.3}$$

where R_s is specular reflection, a' is albedo, x is the distance between the point of observation on the tissue surface and the point of incidence, Δz is the distance between the virtual boundary and the tissue depth, z_b is the distance between the virtual boundary and the tissue surface, and ρ_1 and ρ_2 are the distances between the point

sources and the point of observation. Applying nonlinear least squares fit to the reflectance expression yields the effective attenuation coefficient (μ_{eff}), defined by

$$\mu eff = \sqrt{\frac{\mu_a}{D}} \tag{4.4}$$

The diffusion coefficient can be calculated by

$$D = \frac{\Delta x}{3\sin(\alpha_t)} \tag{4.5}$$

Using Equations 3.2-3.4, the diffuse reflectance profile, and the two-source diffusion theory model, the absorption and reduced scattering coefficients can be calculated by the following equations:

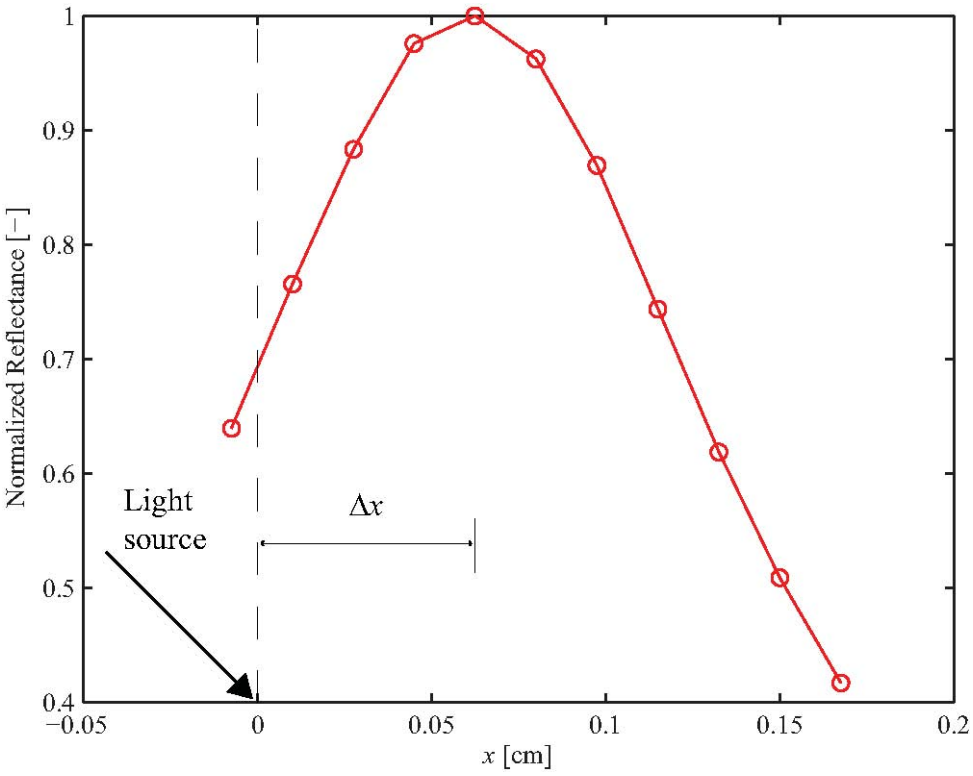

Figure 6. Normalized reflectance profile at wavelength 576 nm used to deduce optical properties

$$\mu_a = \frac{\mu_{eff}^2 \Delta x}{3\sin(\alpha_t)} \tag{4.6}$$

$$\mu_s' = \frac{\sin(\alpha_t)}{\Delta x} - 0.35\mu_a \tag{4.7}$$

4.3 Scalable Monte Carlo

Scalable Monte Carlo allows for a single simulation to be used to fit data and extract optical properties[23]. This method is especially useful for "near diffuse reflectance", when the collection fibers are further than 1 mfp' from the source fibers. If the anisotropy factor and refractive index do not change, it is possible to extract the diffuse reflectance for one set of optical coefficients from one Monte Carlo simulation with another set of coefficients. Using Beer's Law and simulated time-resolved diffuse reflectance, $R_r(\rho,t)$, for certain reference values, μ_{ar} and μ_{sr}, the diffuse reflectance can be obtained for a different absorption parameter, μ_a,

$$R(\rho,t) = R_r(\rho,t)\exp\left[-\left(\mu_a - \mu_{ar}\right)ct\right] \tag{4.8}$$

where *c* is the speed of light. Changing the scattering coefficient alters the photon path length and the time by the scaling factor $\frac{\mu_s}{\mu_{sr}}$. This affects the diffuse reflectance by a power of three; two for the area and one for time.

$$R(\rho,t) = \left(\frac{\mu_s}{\mu_{rs}}\right)^3 R_r\left(\rho\frac{\mu_s}{\mu_{rs}}, t\frac{\mu_s}{\mu_{rs}}\right) \tag{4.9}$$

When both the absorption and scattering coefficients are changed, Equation 4.8 and Equation 4.9 are both used. Applying nonlinear regression, the measured time-resolved

diffuse reflectance can be used to calculate the optical properties of an unknown medium.

CHAPTER V

CLINICAL EXPERIMENT

5.1 Data Collection

Images and histopathological diagnoses were obtained from 250 lesions at the University of Texas M.D. Anderson Cancer Center (Melanoma and Skin Center). Dr. Madeleine Duvic and other dermatologists identified suspicious skin lesions that were going to be biopsied for routine care. Patients were asked to participate in the study and sign an informed consent approved by the IRB under protocol DM98-275. Because the OIR system was built onto a portable cart, it was easily moved to the patient exam rooms. The lights were turned off to remove unknown sources of light. The oblique-incidence spectroscopic probe was used to collect spatio-spectral images from skin lesions and adjacent healthy skin. Baby oil was dropped onto the skin to couple the light in between the probe and the skin. Data was collected with the probe placed perpendicular to the collection site ensuring contact but not compressing the skin. At each position five images are collected, one from each of the source fibers. The probe was rotated 45 degrees and repeated until images of four different probe positions were achieved. A digital image was obtained from each lesion using a Canon camera with an attached Dermlite lens. After the measurements were complete, the physicians removed the lesion and sent it for biopsy. Histopathological diagnoses was performed by UTMDACC and reported within 3 to 4 days.

The lesions included in data analysis include benign common nevi (CN), mildly dysplastic nevi (DN1), moderately dysplastic nevi (DN2), severely dysplastic nevi (DN3), melanoma in situ (M1), invasive melanoma (M2), warts (W), actinic keratosis (AK), seborrheic keratosis (AK), basal cell carcinoma (BCC), and squamous cell carcinoma (SCC). Other lesion types were excluded from data analysis at this time. The categories were separated into two groups, 111 pigmented lesions and 65 non-pigmented lesions. The number of lesions captured and a representative Dermlite image of each type are shown in Table I and Table II. The images show the difficulty that arises when tying to diagnose skin lesions visually. Image acquisition from five source fibers at four probe positions resulted in 20 images being collected from each lesion and corresponding normal tissue. An example spatio-spectral image for normal skin is shown in Figure 7.

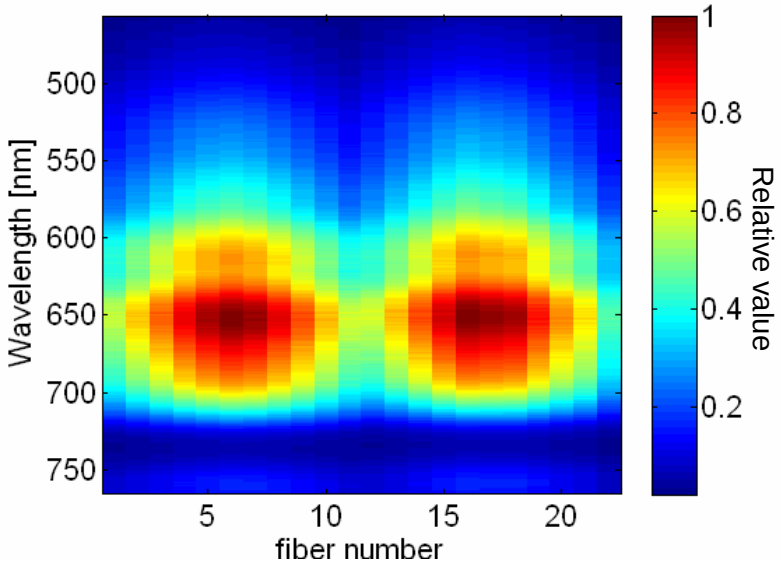

Figure 7. Spatio-spectral image of normal skin

Table I. Pigmented Lesions

Lesion Type	Number of Lesions	Dermlite example image
Common nevi	19	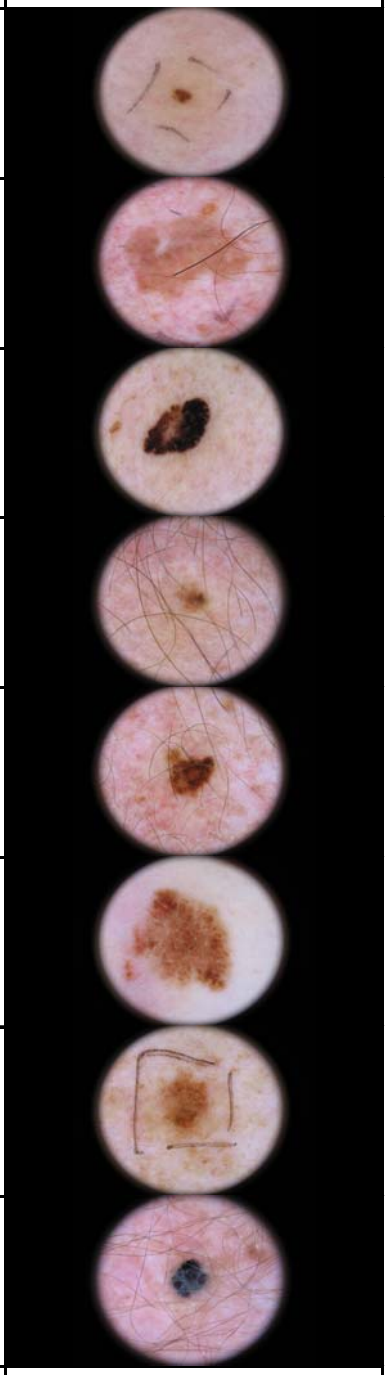
Actinic keratosis	3	
Seborrheic keratosis	12	
Mild dysplastic nevi	21	
Moderate dysplastic nevi	41	
Severe dysplastic nevi	5	
Melanoma	5	
Melanoma in situ	5	
Total	111	

Table II. Non-Pigmented Lesions

Lesion Type	Number of Lesions	Dermlite example image
Common nevi	4	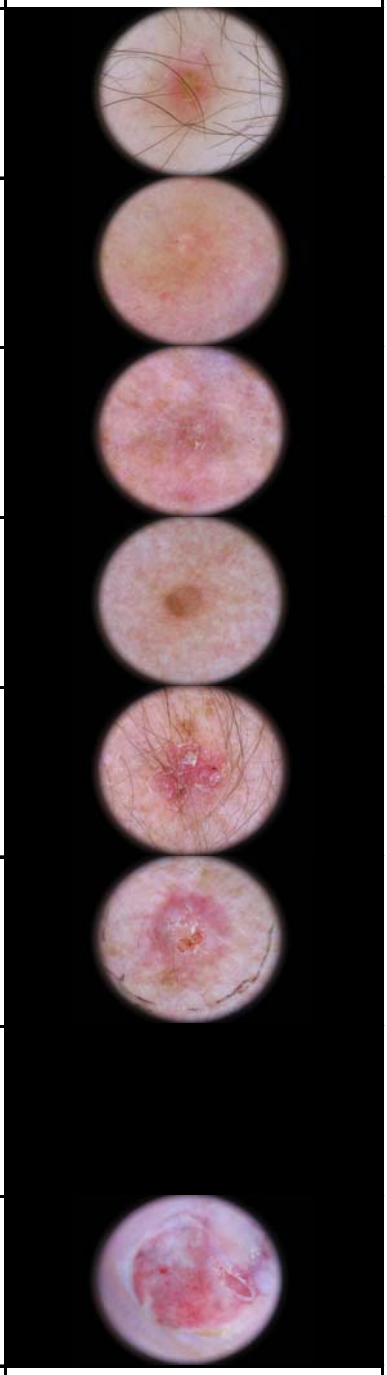
Warts	3	
Actinic keratosis	11	
Seborrheic keratosis	2	
Basal cell carcinoma	28	
Squamous cell carcinoma	14	
Severe dysplastic nevi	1	
Melanoma in situ	2	
Total	65	

5.2 Data Analysis

To classify OIR data, an image processing algorithm was developed and evaluated for both pigmented and non-pigmented lesions. Each lesion image was divided by the related healthy tissue image to normalize the data. This is based on the assumption that the melanin content of healthy skin tissue will correlate with that of the imaged lesion.

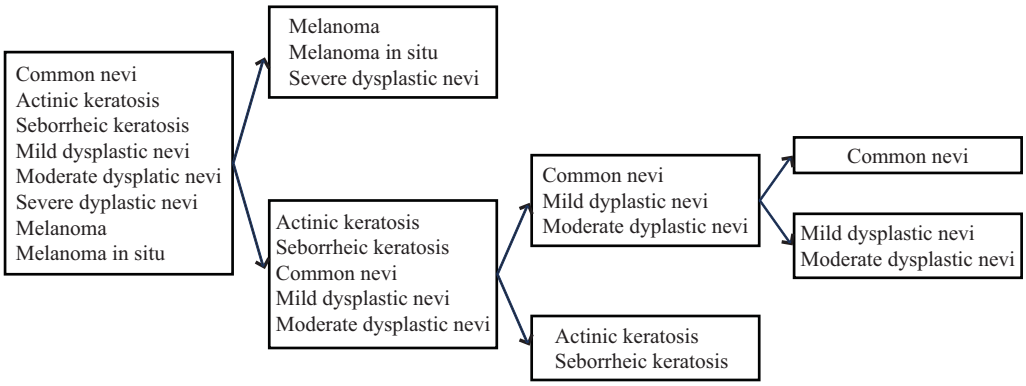

Figure 8. Breakdown of pigmented lesions

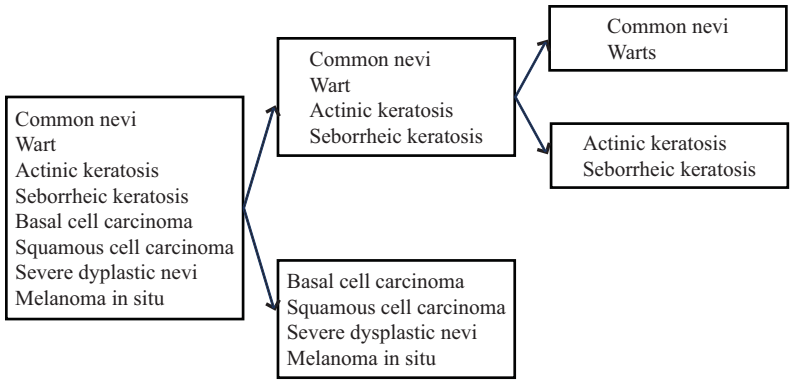

The skin is not homogeneous and will vary within the collection site. To reduce the error, the collection fiber intensity found at each probe position was averaged for each source fiber. For simplification, groups were separated into two classes at a time. Features were extracted from the pigmented lesions to break them into two groups. This was repeated for the subgroups until the desired categories were achieved. The same procedure was followed for the non-pigmented lesions. Figure 8 and Figure 9 illustrate the classification order followed for pigmented and non-pigmented lesions, respectively.

Selection of features

The following describes the method used to establish optimal features for each of the five classifiers. Features were extracted to divide each group in stages. The continuous wavelet transform (CWT) was employed to extract the best five features per fiber in the two classes under analysis. The CWT of $f(t)$ with respect to the wavelet function Ψ is defined as follows[24]:

$$Wf_{\Psi}(b,a) = \frac{1}{\sqrt{a}} \int_{-\infty}^{\infty} f(t)\Psi\left(\frac{t-b}{a}\right)dt\,,\ a<0 \tag{5.1}$$

The Morlet analyzing wavelet was used varying a from 1 to 16 and b along the wavelength range. The one dimensional data, intensity as a function of wavelength, is converted into two dimensional information, wavelet transformation as a function of b and a. CWT features are extracted from the two dimensional data yielding mean, standard deviation, skewness, and kurtosis values for varying wavelength ranges. The five most effective features for each fiber were chosen using the Fisher distance (*FD*) as

a measure of separability between classes. Redundant features were removed from the list and those remaining were narrowed down to the best 20 also using the Fisher distance.

The Fisher distance and the receiver operating characteristic (ROC) curve can both be used as a measure of separability. The results for each measure are comparable though there can be minor differences. The Fisher distance is calculated by

$$FD = |\mu_1 - \mu_2| \sqrt{\sigma_1^{\,2} + \sigma_2^{\,2}} \tag{5.2}$$

where μ_1 and μ_2 denote class means and σ_1 and σ_2 denote class standard deviations. The ROC curve is obtained by plotting the true positive fraction versus the false positive fraction for different cutoff levels. The true positive fraction is when the test is positive and it is correct. The false positive fraction is when the test is positive and it is incorrect. When there is good separation, the area under the ROC curve will be close to 1. This signifies that when the positive tests are correct, there are few incorrect and vice versa.

The Genetic Algorithm (GA) was utilized to find the most effective combination of features. It uses methods of population, crossover, and mutation to find the optimal selection of features[25]. The first population is a random set of chromosomes that represent 1000 possible solutions. According to classification ability, each chromosome is given a fitness value defined as follows

$$\text{Fitness value} = FD * ROCA \tag{5.3}$$

where *ROCA* is the area under the receiver operating characteristic curve. A second population is generated according to the fitness values. Chromosomes that divide classes most effectively are selected to reproduce. The parent chromosomes crossover at

1, 2, or 3 randomly chosen points. The mutation operation randomly changes the offspring resulting from crossover to prevent solutions from falling into a local optimum. This process is repeated until the new population is complete. The generations continue to evolve until a specified condition is satisfied. At this point, the best solution in the final population is chosen as an optimal combination of features. For this study, the program ended, when the fitness value ceased to improve over many generations or a maximum number of generations was reached. This process was repeated several times and the best feature combination was selected. The features included in the first classifier for pigmented lesions are shown in Table III. The others may be found in the Appendix.

Table III. Effective Image Features for First Classifier of Pigmented Lesions

Source Fiber #	Collection Fiber #	Statistic	Wavelength Range	FD	ROCA
sf3	20	mean	542-698	0.9566	0.8434
sf5	14	skewness	560-571	0.8773	0.8240
sf4	3	skewness	560-571	0.8833	0.8108
sf4	21	mean	498-563	0.8875	0.8003
sf5	14	mean	498-563	0.8847	0.7955
sf2	15	mean	563-701	0.8600	0.8090
sf4	4	skewness	542-578	0.8580	0.8073
sf2	14	kurtosis	494-687	0.8437	0.8066
sf3	19	mean	542-756	0.8360	0.8108
sf1	20	mean	542-756	0.8304	0.8059
sf5	20	mean	549-560	0.8176	0.8184
sf4	4	kurtosis	560-571	0.8228	0.7882

Feature conditioning and classification

The resulting features for each classifier were conditioned to remove correlations and reduce dimensionality. Feature vectors were formed for each image based on the chosen effective feature combination. Two steps were necessary to remove correlation. First, the mean feature vector was subtracted. Second, the feature vectors were multiplied by the matrix

$$A_1 = \left(e_1, e_2, ..., e_n\right)^t \tag{5.4}$$

where $\left(e_1, e_2, ..., e_n\right)$ are eigenvectors of the covariance matrix. The within-class matrix (S_B) and the between-class matrix (S_W) were calculated to reduce dimensionality[26].

$$S_W = \sum_{j=1}^{C} \frac{N_j}{N} \sum_{i \in C} \frac{1}{N_j} (x_i - m_j)(x_i - m_j)^T \tag{5.5}$$

$$S_B = \sum_{j=1}^{C} \frac{N_j}{N} (m_j - m_0)(x_j - m_0)^T \tag{5.6}$$

To minimize the separability measure, J, the feature vectors were multiplied by the eigenvector corresponding to the zero eigenvalue of $(S_W{}^{-1}, S_B)$.

$$J = Trace(S_W{}^{-1}, S_B) \tag{5.7}$$

This reduces each feature vector to one dimension based on a new combined image feature (*CIF*) without losing any information.

A Bayes decision rule was used to separate each group based on the selected features. Each classifier categorizes 1 lesion group into 2 subgroups, which for simplicity will be called class I and class II. A lesion is considered to be of class I if

$$\Pr(\text{class I} \mid x) > \Pr(\text{class II} \mid x) \tag{5.8}$$

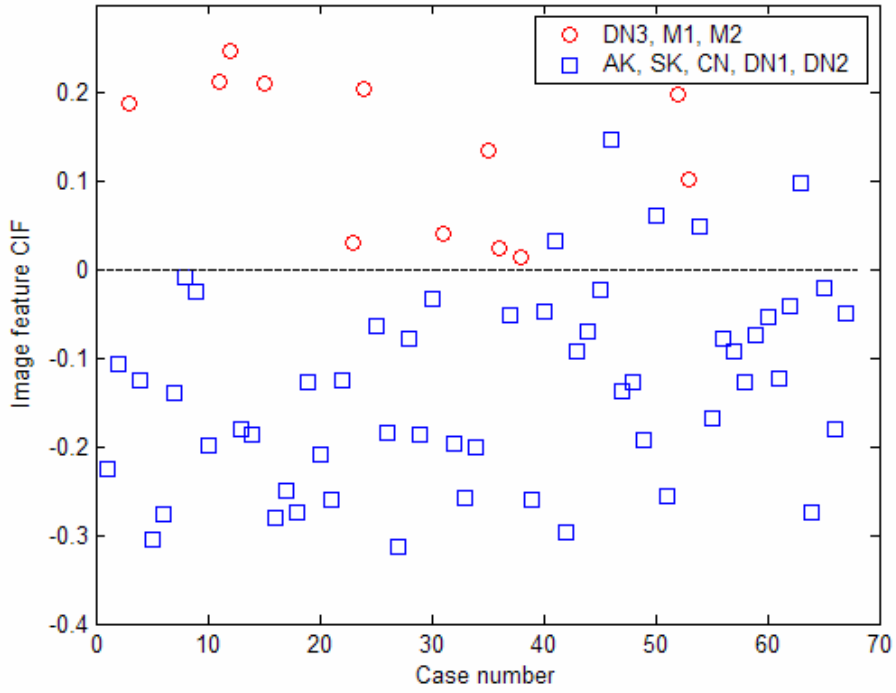

Figure 10. Scatter plot of training data for pigmented lesions

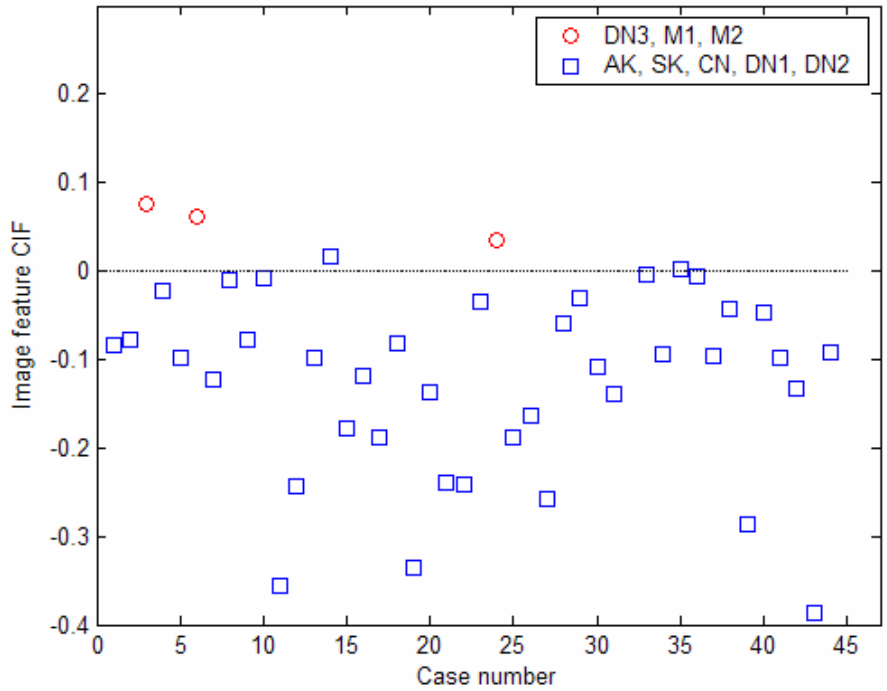

Figure 11. Scatter plot of testing data for pigmented lesions

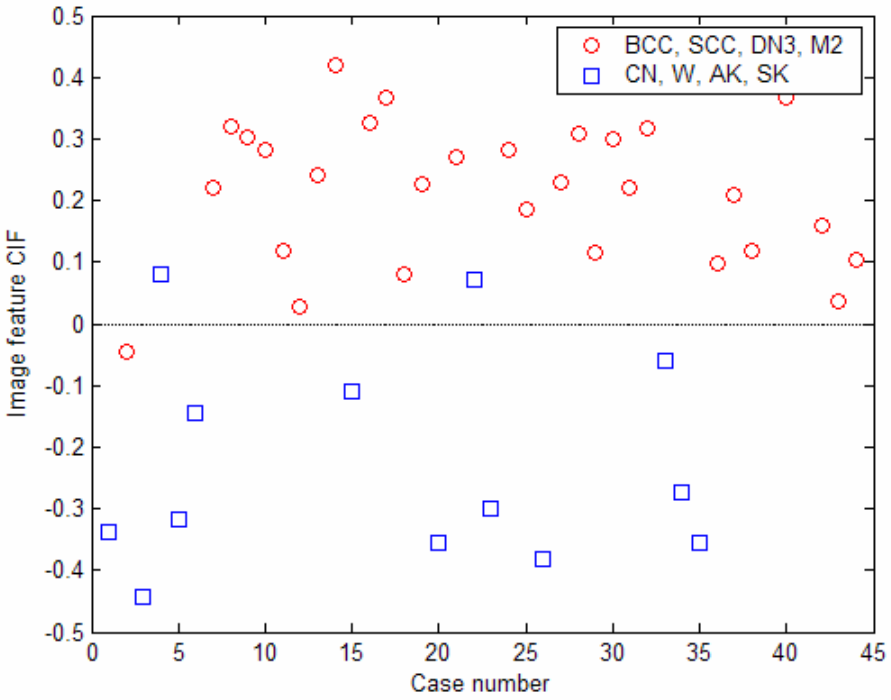

Figure 12. Scatter plot of training data for non-pigmented lesions

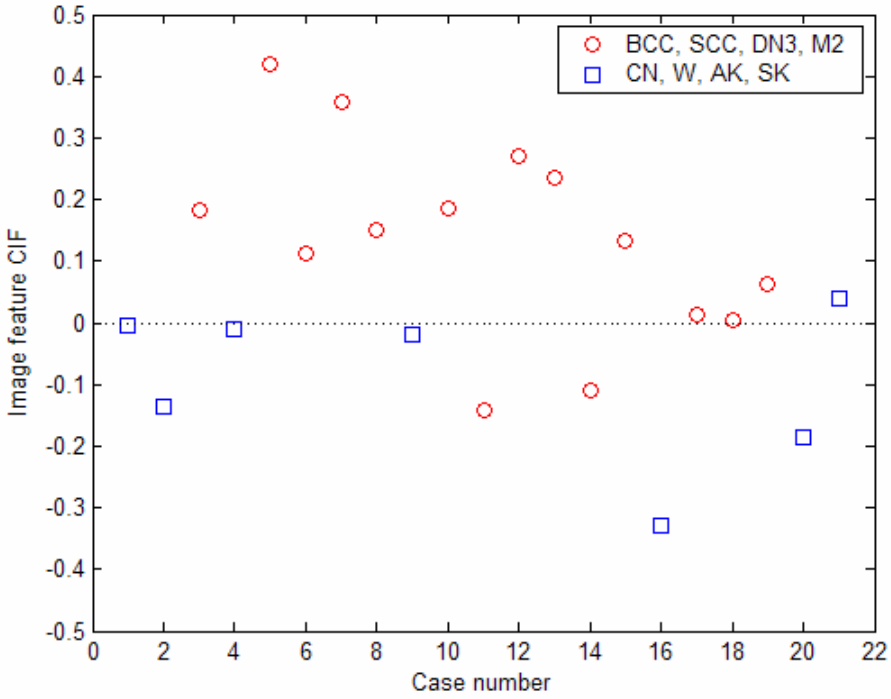

Figure 13. Scatter plot of testing data for non-pigmented lesions

Otherwise, it will belong to class II. Using a one dimensional feature and assuming a Guassian distribution simplifies the criteria. A lesion is considered to be of class I if

$$g \text{ (class I)} > g \text{ (class II)} \tag{5.9}$$

Otherwise, it will belong to class II. The probabilities of a lesion belonging to a certain class for Guassian distributions can be calculated by

$$g \text{ (class I)} = -\ln(\sigma_1) - \frac{(CIF - \mu_1)^2}{\sigma_1} \tag{5.10}$$

$$g \text{ (class II)} = -\ln(\sigma_2) - \frac{(CIF - \mu_2)^2}{\sigma_2} \tag{5.11}$$

where μ_1 and μ_2 denote class means and σ_1 and σ_2 denote class standard deviations. For the training set, the classifier outcome was measured based on histopathology reports.

5.3 Results

Based on the classification features, spatio-spectral images were separated into different categories. The algorithms were evaluated and validated with two thirds of the data as the training set and one third as the testing set. Confusion matrices and classification accuracies are shown in Tables IV-IX. Scatter plots testing and training sets are shown in Figures 10-13. For pigmented lesions, severe dysplastic nevi, melanoma, and melanoma in situ are classified with 100% accuracy in the testing set. The other less severe lesions are classified with accuracies ranging from 84.21-86.67%. There is an overall classification rate of 87.39%. For non-pigmented lesions, basal cell carcinoma,

squamous cell carcinoma, severe dysplastic nevi, and melanoma in situ were classified with 85.71% accuracy in the testing set. The other less severe lesion types were classified with accuracies ranging from 83.33-100%. There is an overall classification rate of 90.77%. Histopathology was used to organize the training set initially and again to measure the classifier with the testing set.

Table IV. Training Confusion Matrix for Pigmented Lesions

	DN3_M1_M2	AK_SK	CN	DN1_DN2	Accuracy
DN3_M1_M2	12				100.00
AK_SK		8			100.00
CN	1	1	9		81.82
DN1_DN2	4		1	31	86.11
Total					89.55

Table V. Testing Confusion Matrix for Pigmented Lesions

	DN3_M1_M2	AK_SK	CN	DN1_DN2	Accuracy
DN3_M1_M2	3				100.00
AK_SK		5		2	100.00
CN		1	7		71.43
DN1_DN2	1	1	2	22	87.50
Total					84.62

Table VI. Overall Confusion Matrix for Pigmented Lesions

	DN3_M1_M2	AK_SK	CN	DN1_DN2	Accuracy
DN3_M1_M2	15				100.00
AK_SK		13		2	86.67
CN	1	2	16		84.21
DN1_DN2	5	1	3	53	85.48
Total					87.39

Table VII. Training Confusion Matrix for Non-Pigmented Lesions

	BCC_SCC_DN3_M2	AK_SK	CN_W	Accuracy
BCC_SCC_DN3_M2	30	1		96.77
AK_SK	1	6		85.71
CN_W	1		5	83.33
Total				93.18

Table VIII. Testing Confusion Matrix for Non-Pigmented Lesions

	BCC_SCC_DN3_M2	AK_SK	CN_W	Accuracy
BCC_SCC_DN3_M2	12	1	1	85.71
AK_SK	1	5		83.33
CN_W			1	100.00
Total				85.71

Table IX. Overall Confusion Matrix for Non-Pigmented Lesions

	BCC_SCC_DN3_M2	AK_SK	CN_W	Accuracy
BCC_SCC_DN3_M2	42	2	1	93.33
AK_SK	2	11		84.62
CN_W	1		6	85.71
Total				90.77

CHAPTER VI

CONCLUSION

For patients with melanoma, finding the tumor early is the key to survival. The current OIR system can image lesions as small as 2 mm in diameter. It can accurately calculate optical properties as compared to estimated values from collimated transmission and Mie theory. It also has good classification results from data collected in recent clinical studies. Data analysis involved lengthy statistical procedures to extract image features. Overall classification accuracies ranged from 84.21-100% for pigmented lesions and 84.62-93.33% for non-pigmented lesions. The pigmented algorithm was able to identify all of the high risk lesions (DN3, M1, M2). Six lesions were incorrectly put into this category, but this is preferable over the problem of classifying high risk lesions as benign. The non-pigmented algorithm classified the high risk lesions (BCC, SCC, DN3, M2) in the testing set with over 85% accuracy. It is likely that the rate is lower due to an increased number of lesions. The next step for this technology is to establish a statistically significant database for different types of skin lesions as well as normal skin. Furthermore, physiological parameters responsible for diagnostic optical features need to be identified. Though it may be some time before any technology can replace the biopsy, OIR could certainly aid the physician in deciding which lesions to biopsy. This could reduce the number of biopsies for benign lesions, as well as help identify lesions that may be dangerous. This technology may be able to bring attention to a lesion that would otherwise be passed up. OIR is a strong competitor with other methods for non-

invasive skin cancer detection. This technology has a promising outlook for skin cancer diagnosis and could also be expanded to ocular, cervical, oral, and GI cancers.

REFERENCES

1. American Cancer Society website. Melanoma and Non-melanoma Skin Cancer. http://www.cancer.org (accessed Sept 13th 2006).
2. L. H. Wang and S. L. Jacques, “Source of Error in Calculation of Optical Diffuse Reflectance from Turbid Media Using Diffusion Theory,” Computer Methods and Programs in Biomedicine 61(3), 163-170 (2000).
3. S. P. Lin, L. H. Wang, S. L. Jacques, and F. K. Tittel, “Measurement of Tissue Optical Properties by the Use of Oblique-incidence Optical Fiber Reflectometry,” Appl. Opt. 36, 136-143, (1997).
4. G. Marquez and L. H. Wang, “White Light Oblique Incidence Reflectometer for Measuring Absorption and Reduced Scattering Spectra of Tissue-like Turbid Media.” Opt. Exp. 1, 454-460 (1997).
5. A. Garcia-Uribe, N. Kehtarnavaz, G. Marquez, V. Prieto, M. Duvic, and L. Wang, “Skin Cancer Detection by Spectroscopic Oblique-incidence Reflectometry: Classification and Physiological Origins”, Optics Letters 43 (13), 2643-2650 (2004).
6. V. P. Wallace, J. C. Bamber, D. C. Crawford, R. J. Ott, and P. S. Mortimer, "Classification of Reflectance Spectra from Pigmented Skin Lesions, a Comparison of Multivariate Discriminant Analysis and Artificial Neural Networks," Physics in Medicine and Biology 45, 2859-2871 (2000).

7. V. P. Wallace, D. C. Crawford, P. S. Mortimer, R. J. Ott, and J. C. Bamber, "Spectrophotometric Assessment of Pigmented Skin Lesions: Methods and Feature Selection for Evaluation of Diagnostic Performance," Physics in Medicine & Biology 45, 735-751 (2000).

8. L. M. McIntosh, R. Summers, M. Jackson, H. H. Mantsch, J. R. Mansfield, M. Howlett, A. N. Crowson, and J. W. Toole, "Towards Non-invasive Screening of Skin Lesions by Near-infrared Spectroscopy", Journal of Investigative Dermatology 116 (1), 175-181 (2001).

9. S. Tomatis, M. Carrra, A. Bono, C. Bartoli, M. Lualdi, G. Tragni, A. Colombo, and R. Marchesini, “Automated Melanoma Detection with a Novel Multispectral Imaging System: Results of a Prospective Study”, Physics in Medicine and Biology 50, 1675-1687 (2005).

10. S. Sigurdsson, P. A. Philipsen, L. K. Hansen, J. Larsen, M. Gniadecka, and H. C. Wulf, “Detection of Skin Cancer by Classification of Raman Spectra”, IEEE Transactions on Biomedical Engineering, no. 10, vol. 51, Oct. (2004).

11. M. Panjehpour, C. E. Julius, M. N. Phan, T. Vo-Dinh, and S. Overholt, "Laser-induced Fluorescence Spectroscopy for in vivo Diagnosis of Non-melanoma Skin Cancers", Lasers in Surgery and Medicine 31, 367–373 (2002).

12. R. G. B. Langley, M. Rajadhyaksha, P. J. Dwyer, A. J. Sober, T. J. Flotte, and R. R. Anderson, “Confocal Scanning Laser Microscopy of Benign and Malignant Melanocytic Skin Lesions in vivo”, J Am Acad Dermatol. 45, 365-376 (2001).

13. K. J. Busam, C. Charles, C. M. Lohmann, A. Marghoob, M. Goldgeiger, and A. C. Halpern, “Dectection of Intraepidermal Malignant Melanoma in vivo by Confocal Scanning Laser Microscopy”, Melanoma Research 12, 349-355 (2002).

14. P. Aberg, I. Nicander, J. Hansso, P. Geladi, U. Holmgren, and S. Ollmar, “Skin Cancer Identification Using Multifrequency Electrical Impedance – A Potential Screening Tool” , IEEE Transactions on Biomedical Engineering 51 (12), 2097-2102 (2004).

15. M. Takahashi, H. Kohda, “Diagnostic Utility of Magnetic Resonance Imaging in Malignant Melanoma”, J Am Acad Dermatol 27, 51-4 (1992).

16. J. Maurer, F. D. Knollmann, D. Schlums, C. Garbe, T. J. Vogl, J. Bier, R. Felix, “Role of High-resolution Magnetic Resonance Imaging for Differentiating Melanin-containing Skin Tumors”, Investigative Radiology 30 (11), 638-643 (1995).

17. G. M. Pennasilico, P. P. Arcuri, F. Laschena, C. Potenza, P. Ruatti, R. Bono, F. Sera, P. Falappa, “Magnetic Resonant Imaging in the Diagnosis of Melanoma: in vivo Preliminary Studies with Dynamic Contrast-enhanced Subtraction”, Melanoma Research 12, 365-371 (2002).

18. V. T. Y. Ng, B. Y. M. Fung, and T. K. Lee, “Determining the Asymmetry of Skin Lesion with Fuzzy Borders”, Computers in Biology and Medicine 35, 103-120 (2005).

19. A. Piantanelli, P. Maponi, L. Scalise, S. Serresi, A. Cialabrini, and A. Basso, “Fractal Characterisation of Boundary Irregularity in Skin Pigmented Lesions,” Med. Biol. Eng. Comput. 43, 436-442 (2005).

20. H. Van de Hulst, *Light Scattering by Small Particles* (Dover Publication, New York, 1983).

21. T. J. Farrell, M. S. Patterson, and B. C. Wilson, “A Diffusion Theory Model of Spatially Resolved, Steady State Diffuse Reflectance for the Noninvasive Determination of Tissue Optical Properties in vivo,” Med. Phys. 19, 879-888 (1992).

22. L. H. Wang and S. L. Jacques, “Use of a Laser Beam with an Oblique Angle of Incidence to Measure the Reduced Scattering Coefficient of a Turbid Medium,” Appl. Opt. 34, 2362-2366 (1995).

23. A. Kienle and M. S. Patterson, “Determination of the Optical Properties of Turbid Media from a Single Monte Carlo Simulation”, Phys. Med. Biol. 41, 2221-2227 (1996).

24. J. Groswami and A. Chan, *Fundamentals of Wavelets, Theory, Algorithms and Application*, 1st ed. (Wiley Interscience, New York 1999).

25. H. Vafaie and K. Jong, “Genetic Algorithms as a Tool for Feature Selection in Machine Learning,” in *Proceedings of the IEEE International Conference on Tools with Artificial Intelligence* (Institute of Electrical Engineers, Piscata Way, N.J., 1992, pp. 200-203).

26. R. O. Duda, P. E. Hart, and D. G. Stork, *Pattern Classification*, 2nd ed. (Wiley Interscience, New York, 2000).

APPENDIX

Table X. Effective Image Features for Second Classifier of Pigmented Lesions

Source Fiber #	Collection Fiber #	Statistic	Wavelength Range	FD	ROCA
sf5	18	skewness	600-763	1.1417	0.8794
sf5	19	mean	592-730	1.0823	0.8704
sf3	18	kurtosis	658-687	1.0329	0.8601
sf1	15	kurtosis	654-687	1.0012	0.8593
sf5	16	kurtosis	661-687	0.9971	0.8477
sf5	14	skewness	647-658	0.9915	0.8391
sf2	19	skewness	600-690	0.9558	0.8362
sf2	21	skewness	600-719	0.9758	0.8136
sf3	21	kurtosis	679-698	0.9371	0.8465
sf3	15	kurtosis	672-763	0.9261	0.8366
sf5	14	kurtosis	658-730	0.9215	0.8379

Table XI. Effective Image Features for Third Classifier of Pigmented Lesions

Source Fiber #	Collection Fiber #	Statistic	Wavelength Range	FD	ROCA
sf3	14	kurtosis	574-603	0.9139	0.8069
sf5	15	skewness	538-611	0.8318	0.8090
sf3	19	kurtosis	520553	0.8224	0.8077
sf5	10	kurtosis	574-603	0.8376	0.7823
sf5	17	skewness	542-571	0.8202	0.7738
sf5	2	skewness	553-563	0.8085	0.7823
sf3	13	kurtosis	542-571	0.7748	0.7937
sf5	11	kurtosis	574-600	0.7058	0.7602
sf1	14	kurtosis	574-603	0.7254	0.7390
sf4	21	kurtosis	600-603	0.7145	0.7453
sf4	18	kurtosis	520-553	0.6934	0.7606

Table XII. Effective Image Features for First Classifier of Non-Pigmented Lesions

Source Fiber #	Collection Fiber #	Statistic	Wavelength Range	FD	ROCA
sf3	21	kurtosis	629-669	0.8253	0.8006
sf5	16	mean	560-752	0.8379	0.8189
sf1	21	skewness	618-672	0.8417	0.8156
sf3	14	skewness	618-676	0.8447	0.8350
sf5	1	mean	538-723	0.8463	0.8100
sf5	17	mean	607-737	0.8474	0.8194
sf3	17	skewness	618-676	0.8508	0.8028
sf3	11	kurtosis	636-665	0.8652	0.8006
sf3	11	skewness	618-672	0.8734	0.8233
sf3	1	mean	538-723	0.8787	0.8067
sf5	5	kurtosis	647-665	0.8924	0.8389
sf3	16	skewness	618-683	0.9004	0.8228

Table XIII. Effective Image Features for Second Classifier of Non-Pigmented Lesions

Source Fiber #	Collection Fiber #	Statistic	Wavelength Range	Final Wavelength	FD	ROCA
sf5	18	skewness	578	607	1.9106	0.9725
sf1	20	skewness	611	621	1.7598	0.956
sf2	20	mean	560	730	1.6391	0.989
sf3	16	mean	527	567	1.6946	0.956
sf2	1	kurtosis	687	708	1.5901	0.9725
sf2	12	skewness	625	661	1.5619	0.9615
sf3	15	mean	560	730	1.4996	0.967
sf2	19	mean	556	589	1.4964	0.9505
sf1	1	skewness	665	748	1.4505	0.9286

VITA

Name: Elizabeth Brooks Smith

Address: 3223 Ashton Park Drive, Houston, TX 77082

Email Address: smitheb@houston.rr.com

Education: B.E., Biomedical Engineering, Vanderbilt University, 2004

M.S., Biomedical Engineering, Texas A&M University, 2006